

Satellite estimation of spectral surface UV irradiance in the presence of tropospheric aerosols

1. Cloud-free case

N. A. Krotkov

Raytheon STX Corporation, Lanham, Maryland

P. K. Bhartia and J. R. Herman

Laboratory for Atmospheres, NASA Goddard Space Flight Center, Greenbelt, Maryland

V. Fioletov and J. Kerr

Atmospheric Environmental Service, Downsview, Ontario, Canada

Abstract. The algorithm for determining spectral UVA (320–400 nm) and UVB (290–320 nm) flux in cloud-free conditions is discussed, including estimates of the various error sources (uncertainties in ground reflectivity, ozone amount, ozone profile shape, surface height, and aerosol attenuation). It is shown that the Brewer-measured spectral dependence of UV flux can be accurately reproduced using just total column ozone amount and the solar flux spectrum. The presence of aerosols tends to reduce the logarithm of the absolute UV flux linearly with aerosol optical depth. Using Brewer measurements of UV flux and aerosol optical depth on clear days at Toronto, the estimated slope falls in the range 0.2 to 0.3 (aerosol single-scattering albedo about 0.95). The Brewer measurements of UV flux can be reproduced using the aerosol model derived within uncertainties of the instrument calibration. We have applied the algorithm to the data collected by the total ozone mapping spectrometer (TOMS) instruments that have been flown by NASA since November 1978. It was demonstrated that in the absence of clouds and UV-absorbing aerosols, TOMS measurements of total column ozone and 380 nm (or 360 nm) radiances can be used in conjunction with a radiative transfer model to provide estimates of surface spectral flux to accuracies comparable to that of typical ground-based instruments. A newly developed technique using TOMS aerosol index data also allows estimation of UV flux transmission by strongly absorbing aerosols. The results indicate that over certain parts of the Earth, aerosols can reduce the UV flux at the surface by more than 50%. Therefore the most important need for reducing errors in TOMS-derived surface UVB spectra is to improve the understanding of UV aerosol attenuation.

1. Introduction

The amount of ultraviolet radiation in the UVA (320–400 nm) and UVB (290–320 nm) spectral ranges that reach the surface of the Earth is determined by Rayleigh scattering from the molecular atmosphere, the absorption of ozone, scattering by clouds, and both scattering and absorption by aerosols. For the last two decades, global increases in UV fluxes from decreasing stratospheric ozone amounts caused by anthropogenic chlorine releasing gases (mostly chlorofluorocarbons) have been an issue of public concern. Changes in UV fluxes at the Earth's surface due to changes of atmospheric ozone content [Stolarski *et al.*, 1991; Herman and Larko, 1994] may strongly affect human health as well as terrestrial and aquatic ecosystems [Scientific Committee on Problems of the Environment (SCOPE), 1992; Smith *et al.*, 1992; SCOPE, 1993; United Nations Environmental Programme (UNEP), 1994; Weiler and Penhale, 1994; International Arctic Science Committee (IASC),

1996]. According to the UNEP [1994] report, a 10% stratospheric ozone reduction will induce about one million new cases of blindness due to cataracts. At the latitudes of middle Europe (50°N) the change has been about 4–6% since 1979. Increased UV radiation may also cause a reduction in crop productivity, and it has been suggested that increased UV fluxes may lead to an increase in the rate of nonmelanoma skin cancer [Leffell and Brash, 1996].

Considerable efforts have been made to understand the spectral UV climatology from ground-based measurements at different locations [World Meteorological Organization (WMO), 1995]. However, the surface UV monitoring stations are sparsely located and have been operating a short time and all are on land. The ground-based measurements have been made using a variety of instruments with varying calibration protocols and stability [WMO, 1995]. On the other hand, UV flux data derived from NASA's TOMS (total ozone mapping spectrometer) satellite instrument are based on a single well-calibrated instrument [Eck *et al.*, 1995; Herman *et al.*, 1996]. Because of long time record (since 1978) and global contiguous spatial coverage the TOMS data are vital for estimating

Copyright 1998 by the American Geophysical Union.

Paper number 98JD00233.
0148-0227/98/98JD-00233\$09.00

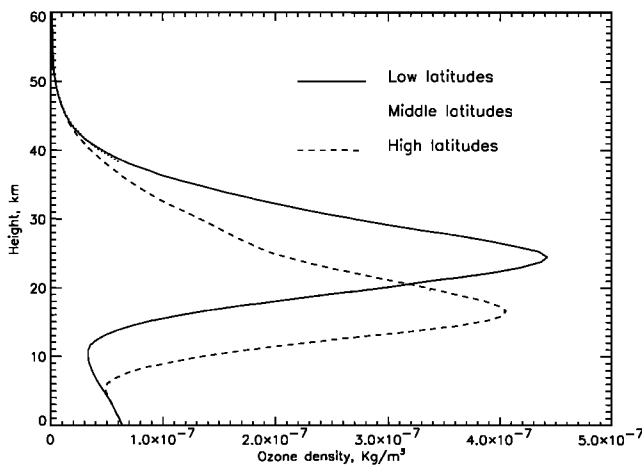


Figure 1. Total ozone mapping spectrometer (TOMS) standard ozone profiles. 325 Dobson units (DU) low-latitude profile (solid line), 325 DU midlatitude profile (dotted line), and 325 high-latitude profile (dashed line). The altitude of the ozone maximum decreases at high latitudes.

trends in surface UV flux [Madronich, 1992; Lubin and Jensen, 1995; Herman *et al.*, 1996]. Using total ozone and 380 nm reflectivity measurements from the TOMS instrument aboard the Nimbus 7 satellite, Herman *et al.* [1996] have estimated the zonal average trends in surface UV flux between January 1979 and December 1992, without regard to possible effects of aerosols. Statistically significant increases in annual UV exposure were found at latitudes above 40° in both hemispheres. For example, at 55°N (United Kingdom, Scandinavia, Canada, Russia) the annual average exposure has increased by 6.8, 8.1, and 4.3% per decade for DNA, plant, and erythral action spectra, respectively. A new TOMS instrument launched on NASA's Earth Probe satellite (first data on July 16, 1996) is expected to continue ozone and surface UV measurements through the end of the century when the last TOMS is scheduled for launch. Additional spaceborne ozone sensors are planned by the United States and other countries well into the next century.

Previous studies of surface UV flux using satellite data [Frederick and Lubin, 1988; Madronich, 1992; Lubin *et al.*, 1994; Lubin and Jensen, 1995; Eck *et al.*, 1995; Long *et al.*, 1996; Herman *et al.*, 1996; Meerkötter *et al.*, 1997] were not focused on the important effects of tropospheric aerosols. In regions where substantial quantities of aerosols are present the surface UV flux will be decreased. The largest decreases in UV fluxes caused by aerosols occur during the summer dry seasons due to smoke from biomass burning in South America and southern Africa and desert dust blowing both east and west from the Saharan region of Africa [Herman *et al.*, 1997].

The purpose of this paper is to present an algorithm for estimating the UV flux at the Earth's surface in a cloud-free atmosphere containing ozone and both absorbing (dust, smoke) and nonabsorbing aerosols. We present a detailed description of the method for calculating the spectral UV flux using TOMS measurements of total ozone and TOMS UV radiances (340, 360, and 380 nm) [Eck *et al.*, 1995; Herman *et al.*, 1996]. This is followed by discussion of the sensitivity of flux to the geophysical parameters (ozone amount, profile shape, tropospheric ozone, surface reflectivity, and surface altitude) and to the aerosol optical parameters. Next, we validate the

results from the radiative transfer model using ground-based spectral measurements from the Brewer instruments at Toronto, Canada. Finally, we discuss the satellite estimation of the surface flux for aerosol-free and aerosol-loaded atmospheres. The detailed effect of clouds will be considered in a future paper.

2. Radiative Transfer Model

Under a cloud- and aerosol-free atmosphere with a Lambertian reflecting surface, the flux at the surface, F_{clear} , can be formally expressed as

$$F_{\text{clear}} = [F_0/d^2](F_{\text{dir}} + F_{\text{diff}})/(1 - R_s S_b) \quad (1)$$

where F_{dir} and F_{diff} are direct and diffuse fluxes at the ground for unit solar flux and zero surface reflectivity; d is the Sun-Earth distance, and F_0 is the extraterrestrial solar flux at 1 AU. The factor $(1 - R_s S_b)^{-1}$ accounts for the effect of surface reflectivity, where R_s is the surface reflectivity and S_b is the fraction of reflected radiation backscattered to the surface by the atmosphere.

To calculate the various terms in (1), numerical solutions of the radiative transfer equation were obtained in the UV spectral region (290–400 nm) by the auxiliary equations method [Dave, 1964], which accounts for all orders of scattering and polarization effects. A spherical geometry correction is applied to the direct component and primary scattered radiation (pseudospherical correction), which allows accurate calculation of surface flux at solar zenith angles up to 85° [Anderson and Lloyd, 1990]. Tables of solution for F_{dir} , F_{diff} , and S_b were calculated for a set of 26 ozone and temperature profiles and for selected values of solar zenith angle (θ_0) and terrain pressure (P_t). These were then used as look-up tables for calculations of F_{clear} (1). The high spectral resolution (0.05 nm) ozone absorption coefficients are based on the laboratory measurements of Bass and Paur [1985], and the Rayleigh scattering coefficients are based on the work by Bates [1984].

The ozone profiles are based on the Nimbus 7 solar backscatter ultraviolet (SBUV) instrument measurements above 15 km and on balloon ozonesonde measurements for lower altitudes [McPeters *et al.*, 1996; Wellemeyer *et al.*, 1997]. Each standard profile represents a multiyear average for a given total ozone bin for all profiles within a latitude band. Profiles have been constructed for three latitude bands: low latitude (15°), midlatitude (45°), and high latitude (75°). These profiles cover a range of 225–475 Dobson units (DU) for low latitudes and 125–575 DU for middle and high latitudes, in steps of 50 DU (1 DU = 1 m atm cm or 2.687×10^{16} O₃ molecules/cm² under standard temperature and pressure conditions). Figure 1 shows the standard 325 DU profiles for low-, middle-, and high-latitude bands.

Sensitivity analysis has shown that the accuracy of radiative transfer flux calculations together with the numerical interpolation technique is better than 1%. Therefore the accuracy for estimating F_{clear} is limited by the uncertainty of the input geophysical parameters: extraterrestrial solar flux F_0 , total column ozone amount Ω , the surface pressure, and reflectivity. Other less sensitive but important parameters include ozone vertical distribution, boundary layer ozone, and SO₂. We examine the sensitivity of the flux to these parameters in the following sections.

2.1. Extraterrestrial Solar Flux

For this study we used the high spectral resolution (FWHM ~ 0.2 nm, sampled approximately every 0.05 nm) extraterrestrial solar flux data obtained from the Solar Stellar Irradiance Comparison Experiment (SOLSTICE) [Rottman *et al.*, 1993] instrument on NASA's Upper Atmospheric Research Satellite (UARS). The two UARS UV solar spectrometers (SOLSTICE and the Solar Ultraviolet Spectral Irradiance Monitor (SUSIM) [Brueckner *et al.*, 1993]) have made daily irradiance measurements since October 1991, a period of time including most of the decrease from the maximum of solar cycle 22 to solar minimum. Daily UV solar spectral irradiance measurements were also made by the solar backscatter ultraviolet/model 2 (SBUV/2) instrument onboard the NOAA 11 satellite between February 1989 and October 1994 [DeLand and Cebula, 1997]. These three independent instruments have shown that the variability of the solar flux (11 year and 27 day) is less than 1% in the near-UV region (290–400 nm). The variation of solar flux with Sun-Earth distance d (about $\pm 3.5\%$ during an annual cycle) is accounted for in (1).

The absolute accuracy of these measurements is maintained through internal calibrations and data set intercomparisons (among SOLSTICE, SUSIM, and SBUV/2 instruments). The measurements by the two UARS instruments were compared with the same-day measurements by three other solar instruments (the solar spectrum (SOLSPEC), the shuttle solar backscatter ultraviolet (SSBUV), and the shuttle SUSIM instruments) during the ATLAS 1 and ATLAS 2 space shuttle missions in March 1992 and April 1993, respectively [Cebula *et al.*, 1996; Woods *et al.*, 1996]. In the 290–400 nm region, at 5 nm spectral resolution, the difference between the various data sets is less than $\pm 3\%$ and is wavelength dependent. Cebula *et al.* [1996] noted that at 1 nm resolution, small errors in wavelength registration can lead to larger differences between in-

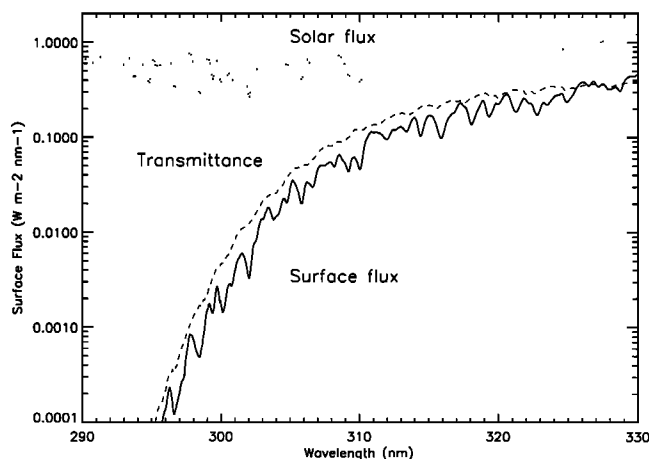


Figure 2. High-resolution (FWHM ≈ 0.2 nm, sampled approximately every 0.05 nm) extraterrestrial solar flux measured by the satellite UARS SOLSTICE instrument (dotted line), calculated atmospheric transmittance (dashed line), and the absolute flux at the surface (solid line) for solar zenith angle 50° , total ozone 275 DU, and surface reflectivity 8%. The sharp decrease of the atmospheric transmittance at short wavelengths results from the spectral features of ozone absorption. The fine spectral structure of the surface flux results from the solar absorption (Fraunhofer) lines.

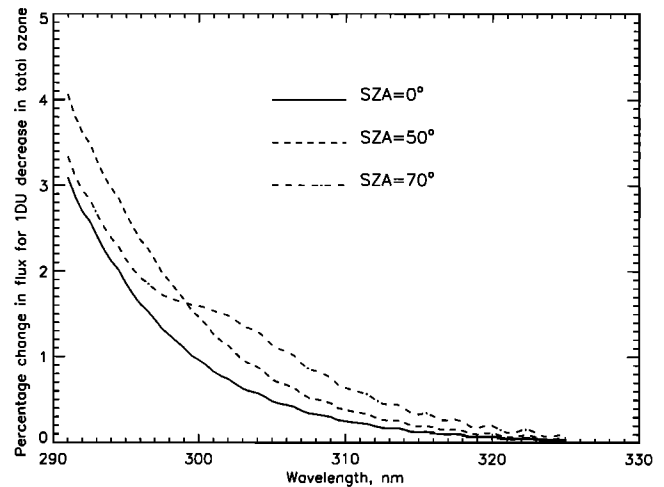


Figure 3. Percentage change in flux for 1 DU decrease in total ozone as a function of wavelength. Total ozone 325 DU and solar zenith angles of zero (solid lines), 50° (dashed lines), and 70° (dashed-dotted lines). Surface reflectivity is 8%.

struments near the vicinity of strong solar absorption features. This problem is exacerbated at higher spectral resolutions.

Figure 2 shows the SOLSTICE solar flux, calculated atmospheric transmittance (F_{clear}/F_0), and the absolute flux at the ground (F_{clear}) at the biologically important wavelengths. The transmittance is a smooth function of wavelength with a sharp decrease at short wavelengths resulting from sharply increasing ozone absorption. Therefore the fine spectral structure of the absolute surface flux F_{clear} results mostly from the solar absorption (Fraunhofer) lines. Using the higher spectral resolution solar spectrum in the model allows better agreement with ground-based spectrometer measurements near the vicinity of Fraunhofer lines [Labow *et al.*, 1998].

2.2. Sensitivity to Total Ozone

Figure 3 shows the percentage increase in flux for a 1 DU increase in total column ozone. Typical errors of 5 DU in measuring total ozone from satellite or ground-based instruments translate into 1–3% error at 310 nm, increasing to 5–8% at 300 nm, and 10–15% at 295 nm. Note that the ozone sensitivity of the flux is a nonmonotonic function of solar zenith angle at short wavelengths. This is due to the fact that when the absorption of the high solar zenith angle direct solar beam becomes very large, most photons reaching the surface are those that have been scattered in the middle stratosphere (20–25 km) and pass to the ground along the shortest vertical path through the ozone layer. This phenomenon is known as the Umkehr effect [Mateer, 1965]. UV flux measurements made by Brewer spectrophotometers at seven Canadian and Japanese stations confirm these model results [Fioletov *et al.*, 1997].

2.3. Effect of Stratospheric Ozone Profile on Surface UV Flux

The surface flux is sensitive not only to column amount but also, to a lesser extent, to the vertical distribution of ozone, particularly at high solar zenith angles. The height of the maximum of the ozone vertical distribution is the most important characteristic of the profile. This height is highly correlated with tropopause height, on the average decreasing from 25 km

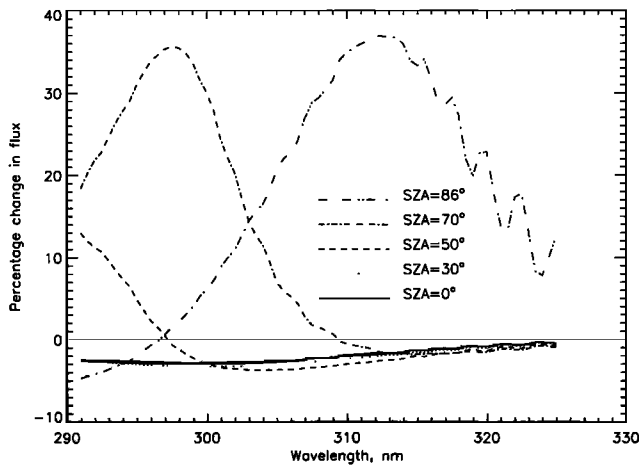


Figure 4. Percentage change in flux when the 325 DU high-latitude ozone profile replaces the 325 DU low-latitude ozone profile. This simulation shows the situation when the altitude of stratospheric ozone maximum decreases by about 10 km, but the total column amount remains unchanged. The surface flux decreases by 3–4% at solar zenith angles less than 50°. For larger solar zenith angle the flux changes from –5 to +40%, due to the Umkehr effect.

in tropics to about 15 km near the poles (see Figure 1). At a given latitude, however, one can have large variability in the ozone profile due to synoptic scale disturbances, which are also associated with variation in the tropopause height. Most of these variabilities are well captured by the total column ozone measurement. The larger the total ozone amount the lower the height of the tropopause and ozone density peak. The combination of latitude and total ozone amount can provide a good estimate of the ozone vertical profile [Klenk *et al.*, 1982, 1983]. Thus the look-up table, described earlier in this section, accounts for a large part of the ozone profile variability one sees in the atmosphere [Wellemeier *et al.*, 1997].

To obtain an upper limit for the errors in UVB flux from ozone profile variability, we compare (Figure 4) the surface UV flux computed from two extreme profiles: the low- and high-latitude ozone profiles that contain exactly the same 325 DU of total ozone (Figure 1). One observes a 3–4% difference in surface flux for solar zenith angles less than 50° and wavelengths longer than 295 nm. The dependence on ozone profile shape becomes significant at $\theta_0 > 60^\circ$, where it ranges from –5 to +40% depending on the wavelength. This complex dependence on the solar zenith angle and wavelength is again related to the Umkehr effect. We note, however, that Figure 4 exaggerates the profile variability seen in practice. The variability of ozone profiles within a latitude band are about one-quarter those from low-latitude to high-latitude profiles or about 1% in surface flux. We also found that variation of surface flux with temperature profile variation is less than with ozone profile variation.

2.4. Effect of Tropospheric Ozone Profile

To investigate the sensitivity of the flux to changes in tropospheric ozone, we modified the standard 325 DU midlatitude ozone profile (Figure 1) by moving 1 DU of ozone from a layer at 16 to 32 mbar to a boundary layer (507–1013 mbar). (Similar perturbations in the upper troposphere produced very little effect and are not discussed). Response of this change is shown

in Figure 5. These results show that for $\theta_0 < 50^\circ$, for a typical 5 DU rms variability in lower tropospheric ozone, the calculated surface flux would have 1σ error of 2% at 300 nm and 0.5% at 310 nm, even if the total column ozone were to be known perfectly. For a long-term increase in tropospheric ozone, this reflects the well-known disproportional role of tropospheric ozone in blocking solar UV radiation [Bruhl and Crutzen, 1989]. At small θ_0 , a given amount of tropospheric ozone absorbs UV radiation more strongly than the same amount of stratospheric ozone because of the longer optical path associated with increased tropospheric multiple scattering. However, at $\theta_0 > 70^\circ$, the stratospheric absorption is more efficient than in the troposphere because most scattering occurs in the stratosphere.

2.5. Surface Reflectivity Effect

Figure 6 shows the percentage change in flux due to increase in surface reflectivity R_s by 0.01. The bottom curves represent conditions for the Earth's surface not covered by ice or snow, when R_s typically vary between 0.01–0.04 (over land) and 0.05–0.08 (over water) [Eck *et al.*, 1987; Herman and Celarier, 1997]. These climatological Lambertian equivalent surface reflectivities (LER) derived from the Nimbus 7/TOMS measurements (1978–1993) are in reasonable agreement with direct ground-based measurements of UV albedo [Blumthaler and Ambach, 1988; Diffey *et al.*, 1995; Feister and Grewe, 1995; McKenzie *et al.*, 1996] (see also a survey by Madronich [1993]). Assuming Lambertian surface, the factor $(1 - R_s S_b)^{-1}$ accounts for the albedo effect on flux (1), where S_b is the fraction of reflected radiation backscattered to the surface by the atmosphere. For low R_s the percentage change in flux is directly proportional to $S_b(\lambda)$. The spectral dependence of $S_b(\lambda)$ has a maximum of about 0.4 around 320 nm, with a decrease longward of the maximum (due to decreasing of Rayleigh optical thickness of the atmosphere), and a sharp decrease shortward (due to the spectral enhancement of absorption by tropospheric ozone). This explains the spectral dependence of the albedo effect. For a Lambertian surface, the effect does not depend on solar angle and only weakly depends on total ozone (Figure 6). For snow-free conditions, when the typical uncer-

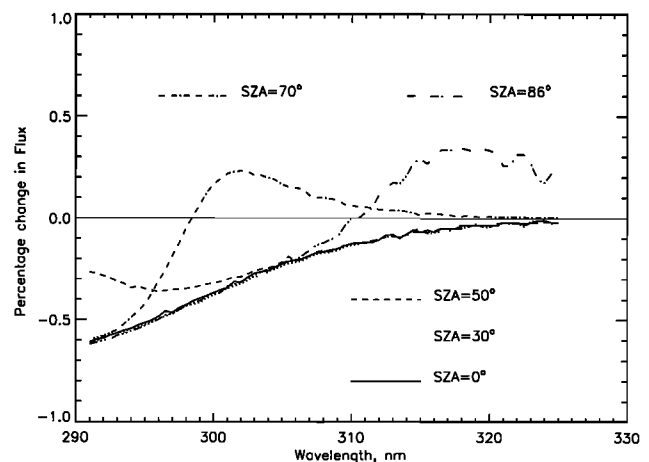


Figure 5. Percentage change in flux due to 1 DU ozone redistribution from Umkehr layer 5 (22.4–25.8 km) to the boundary layer (Umkehr layer 0: 0–5 km). The 325 DU midlatitude standard ozone profile and assumed surface reflectivity of 8%.

tainty in R_s is about 0.02, the maximum error in surface flux (around 320 nm) is less than 1%.

Snow on the ground is the strongest factor that affects the surface albedo and the flux at the ground. The UV albedo of snow varies between 0.2 and more than 0.95 [Blumthaler and Ambach, 1988; Madronich, 1993; Feister and Grewe, 1995]. The highest values of UV albedo ($R_s \sim 0.96$ – 0.98) were measured for Antarctic snow [Grenfell et al., 1994], which were also spectrally flat (within $\pm 1\%$ from 300 nm up to 400 nm). The top curve in Figure 6 represents the effect of Lambertian homogeneous fresh snow surface with $R_s = 0.95$, which is typical for Antarctic or Greenland terrain. Over permanent snow cover (Antarctic, Greenland) the albedo is stable (rms < 5%). The major problems in satellite retrievals remain with the accurate characterization of the angular anisotropy in the distribution of radiation reflected from the snow (G. Jaross, private communication, 1997) and discrimination between snow and clouds [Lubin et al., 1994].

At middle latitudes the flux changes under snow/ice conditions differ at different locations because of the variability in snow/ice albedo and/or horizontal inhomogeneity of the terrain. To quantify this variability, all Canadian Brewer observations taken under clear sky conditions have been divided into two groups: with and without snow cover. It was shown that snow enhances flux at 324 nm by $\sim 39\%$ at Churchill, $\sim 21\%$ at Edmonton, and $\sim 12\%$ at Toronto [Fioletov and Evans, 1997]. These values imply spatially average snow albedos of about 90% (Churchill), 50% (Edmonton), and 30%–40% (Toronto) (Figure 6). Both Edmonton and Churchill are located at rural sites, so the difference is not due to urban influences and is likely due to differences in terrain (flatness, trees). Similar results were obtained by Chubarova et al. [1997] using UV flux

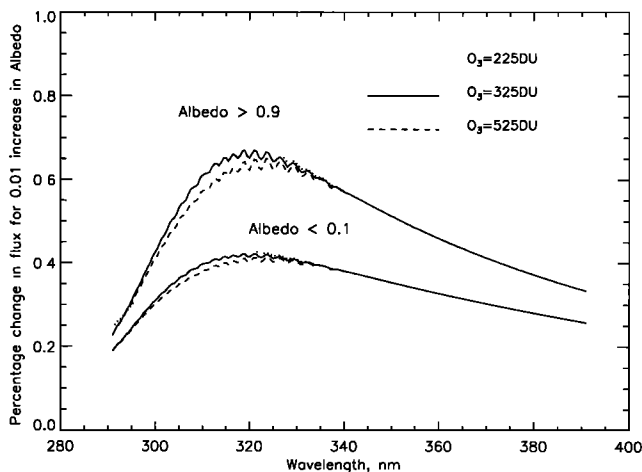


Figure 6. Percentage increase in flux for 0.01 increase in surface albedo R_s . The bottom curves represent the snow-free conditions ($R_s < 0.1$). For Lambertian surface the albedo effect does not depend on solar zenith angle and only slightly on total ozone. The top curves represent the clear sky conditions over homogeneous permanent snow cover (Antarctica, Greenland: $R_s = 0.95$). The percentage change in flux is proportional to the fraction of reflected radiation backscattered to the surface by the atmosphere. The oscillations are due to the band structure in ozone absorption around 320 nm. If the rms variability of R_s is known, the figure can be used to estimate the flux variability over homogeneous surfaces for cloud- and aerosol-free conditions.

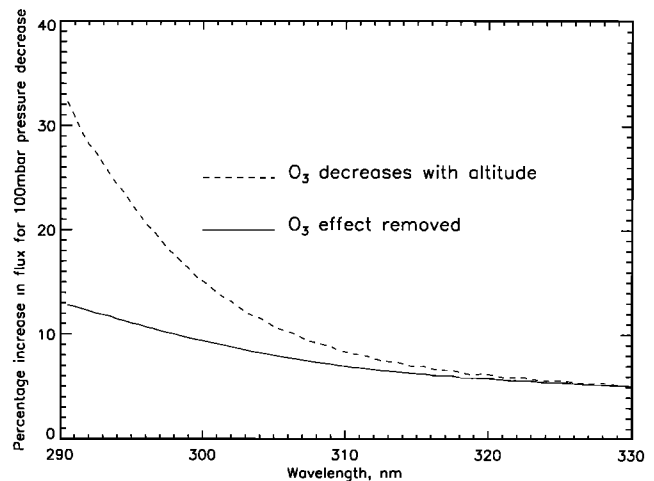


Figure 7. Surface pressure effect. The increase in surface flux due to both decrease in total column ozone, and Rayleigh optical depth (pressure) with altitude is shown by the dashed line for solar zenith angle 50° . The solid line shows only the effect of Rayleigh attenuation and represents the lower limit for the real atmosphere. The percentage flux change is linear with the pressure difference between two levels, and the slope can be estimated from the bottom curve at different wavelengths.

data from the National Science Foundation spectroradiometer at Barrow, Alaska. They have shown more than 50% flux enhancement by snow in the 320–335 nm spectral range. This value implies even greater snow albedo ($R_s > 95\%$). In addition to the site-to-site variability, the albedo at individual sites can vary by about 5–10% depending on the age and depth of snow. If the rms variability of R_s is known, the results from Figure 6 can be used to estimate the corresponding UV flux variability for cloud- and aerosol-free conditions. The presence of clouds enhances the UV flux over that produced by snow under clear sky conditions because of the multiple reflections between the bottom of the cloud and the surface.

2.6. Surface Pressure Effect

Figure 7 shows the effect of surface altitude on UV flux. The increase in surface flux is due to both the decrease in total column ozone and in Rayleigh attenuation with altitude. Since the total ozone column above the surface is typically known when one estimates the UV flux, we consider only the second component, shown by the solid line. The decrease in Rayleigh attenuation with altitude causes the direct flux to increase and diffuse flux to decrease. The global flux (direct plus diffuse) increases with altitude. The logarithm of the flux changes approximately linearly with surface pressure. Therefore the percentage change in flux between any two levels in the atmosphere is proportional to the pressure differences between these levels. Figure 7 shows the proportionality coefficient as a function of wavelength (solid line). In a cloud- and aerosol-free atmosphere the flux at 300 nm increases by about 10% per each 100 mbar pressure decrease (5% at 330 nm). This is the lower limit for the real atmosphere. The flux increases even more if boundary layer aerosol or albedo changes are taken into account [Blumthaler et al., 1994].

2.7. Effect of Aerosols on Surface UV Flux

We shall describe the aerosol effect on global (direct plus diffuse) UV flux by an aerosol attenuation factor (η), defined as follows:

$$F_{\text{aer}} = F_{\text{clear}}(1 - \eta) \quad (2)$$

where F_{aer} and F_{clear} are fluxes for aerosol-loaded and aerosol-free atmospheres. In a study by Kerr [1997], variations in UV flux measured on clear days at Toronto with a Brewer instrument 14 were compared with aerosol optical depth (τ_a) measurements made with the same instrument. The analysis found that the dependence of η on τ_a can be fitted to the expression

$$\eta = 1 - \exp(-k\tau_a) \quad (3)$$

where k falls in the range 0.2 to 0.3. We use radiative transfer calculations to examine (3) for different aerosol models (Table 1) embedded in a Rayleigh atmosphere with ozone. For each aerosol model, the values of $F_{\text{aer}}(\lambda)$ and k were calculated and validated over a wide range of observational conditions using different radiative transfer codes (DISORT code of Stamnes *et al.* [1988]), modified versions of the Vector Program D (VPD) code [Dave, 1978], and the Gauss-Seidel code [Herman and Browning, 1965]). Calculations using the properties of nonabsorbing aerosols (anthropogenic sulfate, maritime) show that they have small effects on the UV flux ($k < 0.15$). This can be explained by the fact that the decrease in direct solar flux caused by aerosol extinction is approximately compensated by an increase in diffuse sky flux caused by aerosol scattering. For UV-absorbing aerosols (dust, smoke, and urban) the increase

Table 1. Description of Tropospheric Aerosol Models Used in This Study

Model	Reference	ω (325)	k (325), SZA = 30°
Sulfate	[Shaw, 1979; Beyer <i>et al.</i> , 1996]	1	0.1
Maritime	[WMO, 1986]	0.98	0.15
Toronto	[Kerr, 1997]	0.95	0.2
Continental	[WMO, 1986]	0.9	0.3
Dust 1	[Patterson <i>et al.</i> , 1977; d'Almeida, 1987]	0.82	0.4
Urban	[WMO, 1986]	0.66	0.5
Dust 2	[Patterson <i>et al.</i> , 1977; Schütz, 1980]	0.6	0.63

SZA, solar zenith angle. The sulfate model is representative of the nonabsorbing tropospheric aerosols of anthropogenic origin [Shaw, 1979]. The refractive index is prescribed on the basis of laboratory measurements at UV wavelengths [Beyer *et al.*, 1996]. Dust models are based on the UV refractive index measurements of Saharan aerosols by Patterson *et al.* [1977]: Dust 1 is representative of the nucleation mode [d'Almeida, 1987], and Dust 2 is representative of larger dust particles [Schütz, 1980]. The Toronto aerosol model was developed to fit the measurements of Kerr [1997] (see section 3.2). The WMO [1986] models (maritime, continental, and urban/industrial) are given for reference. No data are available on the UVB refractive index for carbonaceous aerosols representative of South American or African biomass burning smoke. However, away from the source regions and for the 340–380 nm spectral range, the optical properties of weakly absorbing smoke were shown to be similar to the optical properties of the background dust model (Dust 1 model is similar to D1 model of Torres *et al.* [1998]). The aerosol optical parameters (single-scattering albedo ω , extinction coefficient, phase matrix) were calculated assuming the particles are spherical. The values of flux sensitivity to aerosol optical depth $k = -\partial \ln(F_{\text{aer}})/\partial \tau_a$ at 325 nm are given for solar zenith angle 30° and unit aerosol optical depth: $k(325) = 0.1 + 2(1 - \omega) - 2(1 - \omega)^2 \pm 0.04$.

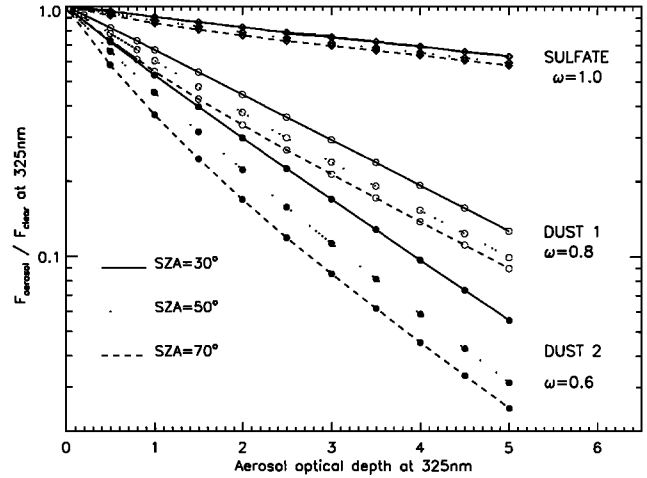


Figure 8. Total transmittance of aerosol loaded atmosphere with respect to the aerosol-free atmosphere ($F_{\text{aer}}/F_{\text{clear}}$) as a function of aerosol optical depth at 325 nm. The presence of aerosols tends to reduce the logarithm of the flux linearly with aerosol optical depth. The slope, $k = -\partial \ln(F_{\text{aer}})/\partial \tau_a$, increases with aerosol absorption (single-scattering albedo: $1 - \omega$) and solar zenith angle.

in the diffuse flux is decreased by aerosol absorption. The effect on global flux is therefore mainly controlled by the aerosol absorption to extinction ratio determined by the single-scattering albedo $1 - \omega$. For tropospheric models presented in Table 1 the dependence of k on $(1 - \omega)$ can be fitted to the expression $k = 0.1 + 2(1 - \omega) - 2(1 - \omega)^2 \pm 0.04$ (at $\theta_0 = 30^\circ$ and $\lambda = 325$ nm).

To test parameterization (3), the values of F_{aer} were calculated for a range of τ_a and solar zenith angles θ_0 . Figure 8 shows the model dependencies of $\ln(F_{\text{aer}}/F_{\text{clear}}) = \ln(1 - \eta)$ on τ_a at 325 nm for different θ_0 and aerosol models. The presence of aerosols tends to reduce the logarithm of the UV flux linearly with aerosol optical depth. The slope $k = -\partial \ln(F_{\text{aer}})/\partial \tau_a$ increases with aerosol absorption ($1 - \omega$) and solar zenith angle. The dependence is quantified in Table 2 where average k values are given with intervals of variation. We note that for absorbing aerosols and $\theta_0 > 50^\circ$, k increases for small τ_a . The value of $k \approx 0.2$ at 325 nm and $\theta_0 = 50^\circ$ was estimated based on the Brewer 14 measurements of UV flux and aerosol optical depth on clear days at Toronto [Kerr, 1997]. This value implies a prevailing aerosol single-scattering albedo of about 0.95.

Figure 9 shows the spectral dependence of the aerosol attenuation factor $\eta(\lambda)$ for aerosol models described in Table 1 and unit optical depth at 325 nm. For strongly absorbing aero-

Table 2. Values of Flux Sensitivity to Aerosol Optical Depth $k = -\partial \ln(F_{\text{aer}})/\partial \tau_a$ at 325 nm for Different Solar Zenith Angles and Aerosol Models

Aerosol Model	Solar Zenith Angle			
	$\theta_0 = 0^\circ$	$\theta_0 = 30^\circ$	$\theta_0 = 50^\circ$	$\theta_0 = 70^\circ$
Sulfate	0.082 ± 0.002	0.095 ± 0.005	0.12 ± 0.02	0.14 ± 0.03
Dust 1	0.34 ± 0.02	0.41 ± 0.01	0.48 ± 0.03	0.54 ± 0.08
Dust 2	0.55 ± 0.04	0.62 ± 0.04	0.76 ± 0.07	0.9 ± 0.2

Larger values of k correspond to small aerosol optical depths: $\tau_a < 1$.

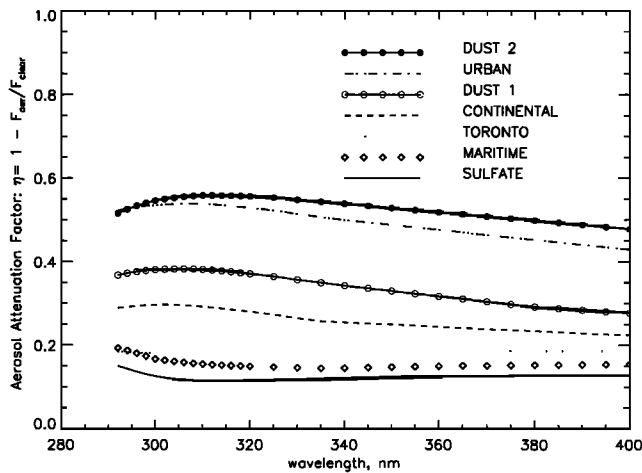


Figure 9. Spectral dependence of the aerosol attenuation factor $\eta(\lambda) = 1 - F_{\text{aer}}(\lambda)/F_{\text{clear}}(\lambda)$ for clear atmosphere with embedded aerosols (aerosol models are described in Table 1). Solar zenith angle is 50° , surface albedo 5%, and unit optical depth at 325 nm for all models. The aerosol attenuation is spectrally flat for weakly absorbing aerosols ($\omega > 0.9$).

sols (dust, urban), η increases at short wavelengths because of the typical increase in the imaginary part of the refractive index at short UVB wavelengths [Patterson *et al.*, 1977] (see also survey by Sokolik *et al.* [1993]). However, for more widespread weakly absorbing aerosols ($\omega > 0.9$) the wavelength dependence of $\eta(\lambda)$ is small in the 300–400 nm region. The spectral gradient of aerosol attenuation can therefore be inferred from the measurements in the UVA spectral region where the ozone effect is negligible (Figure 3). To do so, it is important to have spectral flux measurements at longer UVA wavelengths [Mayer *et al.*, 1997]. Understanding the behavior of η could also be achieved relatively inexpensively by deploying many broadband UVA instruments at different sites around the world.

3. Comparisons With Ground Data Sets

The sensitivity study conducted in the previous section gives a theoretical estimate of the model errors for simplified atmospheric conditions. Comparisons with the ground-based UV flux measurements are necessary to characterize the model uncertainties for the real atmosphere. For the model comparison with the measurements, adaptation of the model to the particular instrument is necessary, including correction for the difference between the spectral bandwidths of model and measurement (see the discussion by Mayer *et al.* [1997]). This correction can be achieved when the high spectral resolution model flux is degraded using the instrument's slit function. Although the slit function for a particular instrument may be more or less well characterized, the wavelength registration may not be known perfectly. This is the main problem in intercomparisons of low spectral resolution flux measurements with the model results.

Figure 10 shows the flux sensitivity to wavelength shift of 0.1 nm at different spectral resolutions simulating measurements taken with spectroradiometers (≈ 0.5 nm for Brewer instrument) to filter instruments (≈ 5 nm). At high spectral resolution, errors of 5–10% are possible near the solar Fraunhofer lines throughout the entire UV spectral region. Although at low spectral resolution the effect of Fraunhofer lines averages

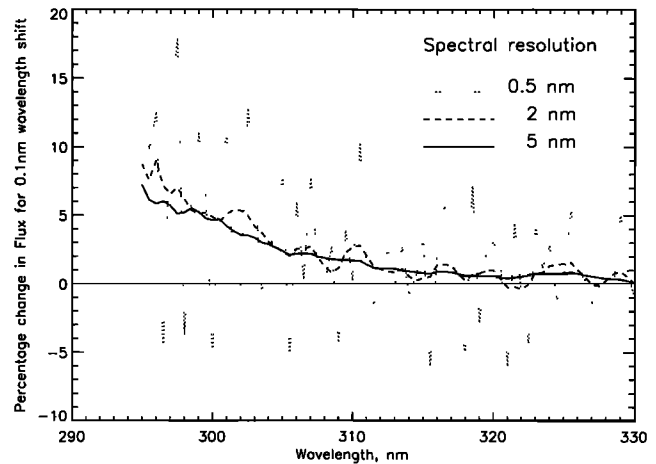


Figure 10. Percentage change in flux for 0.1 nm shift in wavelength at different spectral resolutions simulating the measurements taken with spectroradiometers (Brewer instrument ~ 0.5 nm) to filter instruments (~ 5 nm). At high spectral resolution the errors of 5–10% are possible near the solar Fraunhofer lines throughout the entire UV spectral region. At low resolution the flux is still sensitive to wavelength shift in UVB region, because of the sharp increase in ozone absorption.

out, F_{clear} remains very sensitive to small wavelength errors, ranging from 2% at 310 nm to 8% at 295 nm. Measurements over a near-erythemal action-spectrum weighted flux (e.g., Robertson-Berger meters) have an uncertainty of 2.5% for 0.1 nm error in wavelength. Since it is very difficult to calibrate low spectral resolution radiometers to an accuracy of 0.1 nm, or to maintain them to such relative accuracy over long periods, wavelength uncertainties are one of the chief sources of error in using these broadband radiometers for comparisons with the model.

3.1. Comparisons of Flux Ratios With Brewer Measurements for Cloud-Free Conditions

The results of our model calculations of surface flux were compared with double monochromator Brewer spectrophotometer UVB flux spectral observations (see Figure 11). The comparisons were done under conditions without snow or ice. The spectra were measured at Toronto in 1995 and 1996 by Brewer instrument 21. Since the predicted wavelength dependence of aerosol and surface reflectivity effects is small in the 300–325 nm region, the wavelength dependence of UVB flux is almost entirely due to the wavelength dependence of clear sky flux.

To study the spectral dependence of UVB flux, ratios were calculated between the UV flux at each wavelength in the range 290–325 nm and the UV at 324 nm for both the Brewer measurements and the model data sets (hereinafter referred to as “normalized spectra”). To minimize cloud effects, only days with at least 80% clear sky flux were used. Practically, it means the ground-observing conditions were mostly clear sky, some broken clouds with bright Sun, or very thin (cirrus) clouds. Then, data were filtered by total ozone. Only the days with the measured daily mean total ozone between 280 and 320 DU were selected for comparison. These ozone values are typical for northern midlatitudes in summer. Total ozone was measured by a direct Sun technique using a different Brewer instrument (14).

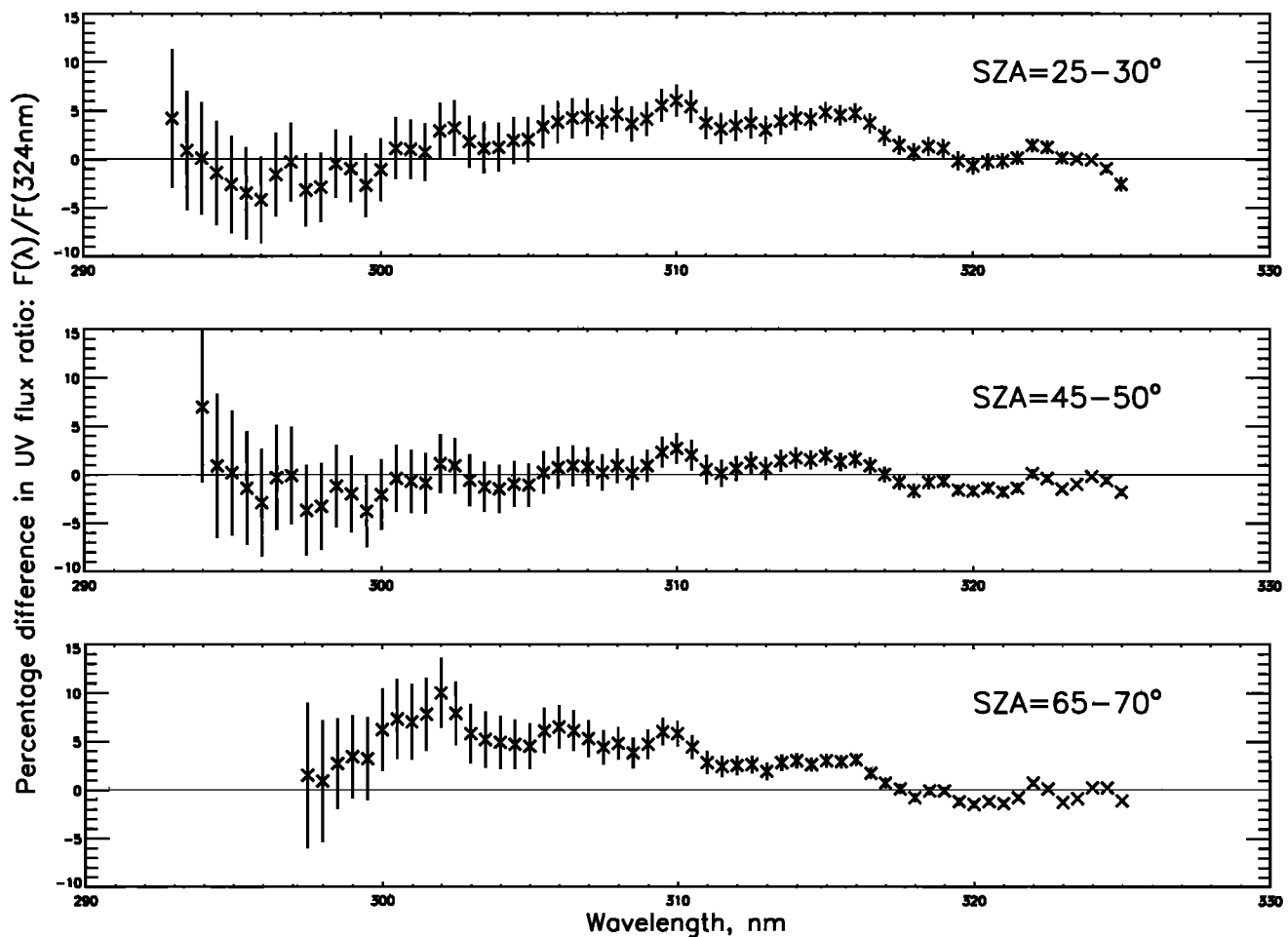


Figure 11. Brewer measurements versus clear sky model comparisons of the normalized total flux ratio: $F_{\eta} = F_{\lambda}/F_{324}$. Both Brewer and model data were smoothed over 1.5 nm. The mean percentage differences, $(F_{\eta \text{ Brewer}} - F_{\eta \text{ model}})/F_{\eta \text{ model}}$, are shown with stars. The error bars show $\pm 2\sigma$, where σ is the standard error of the mean difference for smoothed data.

Next, the Brewer data were binned into 5° intervals of solar zenith angle. The average total ozone was calculated for each bin. It was found that for zenith angles between 20° and 30° the measurements were taken on days whose mean total ozone was approximately 307 DU. For all other zenith angle intervals the average of the measured total ozone values was close to 300 DU. The model spectra were calculated for the average total ozone amount for each solar angle bin, cloud- and aerosol-free conditions, and 5% surface reflectivity for solar zenith angles from 20° to 85° with 1° increment. The model data were degraded using an idealized Brewer instrument triangular slit function with 0.5 nm half-band width, which could result in some differences between the model and the measurements at certain wavelengths near strong solar Fraunhofer lines (Figure 10). To reduce the Fraunhofer line effect, both measured and modeled spectra were smoothed using a 1.5 nm rectangular filter.

Each measured normalized spectrum was matched to the degraded modeled spectrum for the nearest solar zenith angle. At each wavelength the percentage difference between the measured and the modeled normalized spectra was calculated. The differences were grouped into 5° intervals of solar zenith angle to calculate means and standard deviations.

Results of the comparison are shown in Figure 11 for solar

zenith angle bins of 25° – 30° (62 data points), 45° – 50° (96 data points), and 65° – 70° (136 points). In the range 300–325 nm for $\theta_0 = 20^{\circ}$ – 50° and for ozone values around 300 DU (280–320 DU) the mean difference between the model and the measured normalized fluxes is within 5%. For shorter wavelengths the difference is larger, especially for $\theta_0 > 60^{\circ}$. More detailed comparisons with other Canadian Brewer instruments yield similar results [Labow *et al.*, 1998]. The agreement between calculated and measured normalized spectra means that given the measured flux at one UVA wavelength (324 nm) and total ozone (from TOMS or the Brewer instrument), the UVB spectral flux can be accurately estimated to within 5% for the range 300–325 nm.

3.2. Comparisons of UV Fluxes (323–325 nm) With Brewer Measurements

The comparisons of absolute fluxes is a more difficult task. Simulated Brewer spectra (290–325 nm at 0.5 nm increments) were generated by the forward radiative transfer model (section 2) for each Brewer 14 measurement taken at Toronto, Canada, from January 1989 to May 1993. Of the approximately 12,900 measurements taken during this period, nearly 4400 were made on 456 days when the satellite (TOMS) reflectivities were below 17%. To discriminate between partial cloud

cover and high aerosol contaminated days, direct observations of cloud cover are necessary. Special care has been taken to select only clear sky days from all Brewer measurements based on the meteorological reports from Toronto airport (T. Eck, private communication, 1997). In addition, the comparisons were done under conditions without snow and ice. Only about 30 clear days were selected for this initial comparison of the absolute fluxes (the same data set used in the Kerr [1997] analysis), and only one near-noon UV spectrum was taken for each of these days. The averaged spectrally integrated UV flux from 323 nm to 325 nm was compared for both measured and calculated data sets. It is important to note that this averaging reduces the error in the model calculations if the values of the Brewer slit widths are not known precisely. If the ozone value is slightly in error, only a small bias will be introduced into the calculated average since the longer wavelength end of the spectrum is least affected by errors in the total column ozone amount.

The aerosol correction was applied to the model clear sky flux on the basis of the Brewer-measured aerosol optical depths at 315 nm and three different aerosol models (Table 1). The percent difference between the model and the measurements is shown in Figure 12 as a function of aerosol optical depth. One can see progressively better results as aerosol absorption decreases (ω gets larger). The Toronto aerosol model results with $\omega = 0.95$ (or $k = 0.2$ at 325 nm as measured by Kerr [1997] for Toronto) show little dependence on aerosol optical depth but are on average $\sim 8\%$ higher than measured values. This difference cannot be explained by any other reasonable aerosol model with different ω , especially at low optical depths ($\tau_a < 0.3$). A likely cause for the 8% bias between the model and the observations is the known difference between the angular response of the Brewer instrument and the ideal cosine response. An ideal instrument would respond to radiation in proportion to the cosine of the angle between the vertical and the direction of incidence. In practice, most instruments do not follow a true cosine response [Mayer et al., 1997]. The measured angular response of Brewer instrument 14 is less than the cosine curve, and therefore the irradiance measured by the instrument is less than that falling on a horizontal surface and a positive correction is required. It is estimated that the correction required for Brewer 14 is about $+6\% \pm 2\%$ depending on the angular distribution of the incident radiation. After the correction an average systematic difference between measurement and model becomes less than 4%. This is comparable to the uncertainty of extraterrestrial solar flux data and variability seen from Brewer absolute calibrations [Kerr, 1997]. Similar results were obtained in other comparisons between the modeling results and the best ground-based observations in the 300 to 330 nm spectral range [Mayer et al., 1997; Weihs and Webb, 1997, and references therein]. We show the model comparisons with different Brewer instruments under a wide variety of conditions in a separate paper [Labow et al., 1998].

4. Satellite Estimation of Surface UV Flux

We now apply the surface UV estimation technique developed in section 2 to the data collected by the total ozone mapping spectrometer (TOMS) instruments that have been flown by NASA since November 1978 [Eck et al., 1995; Herman et al., 1996]. This 17 year data record (with gaps in 95–96) is the only satellite ozone and radiance data set of its kind. The

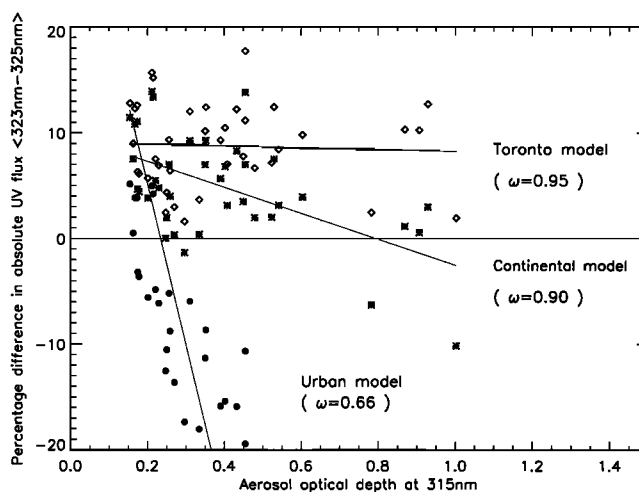


Figure 12. Brewer/model comparisons of the UVA absolute flux: (Model-Brewer)/Brewer, %. The flux is averaged over 323–325 nm spectral range. Model data include the aerosol attenuation factor calculated on the basis of the Brewer-measured aerosol optical depth (315 nm) and three different aerosol models: Toronto (diamonds, $\omega = 0.95$), WMO continental (stars, $\omega = 0.90$), and WMO urban (circles, $\omega = 0.66$) (see Figure 9 and Table 1). The Toronto aerosol model results with $\omega = 0.95$ (or $k = 0.2$ as measured by Kerr [1997]) shows a little dependence on τ_a but are $\sim 8\%$ higher on average than the measured values. This can be explained by the known difference between the angular response of the Brewer instrument and the cosine response (the Brewer data should be increased by $6\% \pm 2\%$ depending on the angular distribution of the incident radiation).

long-term accuracy in measuring total column ozone from this instrument series has been estimated to be $\sim 1\%$ /decade [Wellemeyer et al., 1996, 1997].

Estimation of surface UV flux from TOMS has three components.

1. Surface fluxes expected in aerosol-/cloud-free conditions are estimated using (1) with TOMS-measured total ozone, a climatological database of UV surface reflectivity [Herman and Celarier, 1997], terrain height database [Wieser, 1987], and extraterrestrial solar flux obtained from UARS/SOLSTICE instrument (as described in section 2.1) shifted to air wavelengths.
2. The flux is adjusted for thin cloud or nonabsorbing aerosol effects using the radiances measured by TOMS at a nonozone-absorbing wavelength band (340, 360, or 380 nm) and TOMS climatology of the true surface reflectivity at these wavelengths [Herman and Celarier, 1997].
3. We make preliminary estimates of the effects of UV-absorbing aerosols on surface UV, using a recently developed TOMS residue or aerosol index (AI) [Herman et al., 1997; Torres et al., 1997].

4.1. Cloud-/Aerosol-Free Case

Table 3 provides a summary of errors in the estimation of surface flux at 310 nm from TOMS at different solar zenith angles for cloud- and aerosol-free conditions based on radiative transfer calculations.

We note the following: (1) Numbers in parentheses apply to snow/ice conditions for horizontally homogeneous surfaces with high surface albedo, $R_s > 0.9$ (Antarctic, Greenland).

Table 3. TOMS Errors in Estimated Surface Flux at 310 nm for Cloud- and Aerosol-Free Conditions

Error Source	SZA = 0°	SZA = 50°	SZA = 70°	SZA = 86°
Total ozone, 2% rms	1.3%	2%	3%	<3% (Umkehr)
Surface reflectivity snow-/ice-free, 1% rms (*snow/ice, 5% rms)	0.4% (3%)	0.4% (3%)	0.4% (3%)	0.5% (3%)
Stratospheric profile (1/4 of high-low difference)	0.5%	0.7%	0.3%	>30% (Umkehr effect)
Tropospheric profile (5 DU rms)	0.5%	0.5%	0.2%	0.2%
Total rms	2% (3.6%)	2.8% (4%)	3.7% (4.7%)	>30%

The table concerns only cloud- and aerosol-free cases and gives lower limits of the uncertainties for horizontally homogeneous scenes over TOMS footprint (50 km × 50 km at nadir for Nimbus 7/TOMS instrument). The effects of subpixel variability within TOMS footprint are not considered.

*The number refers to the permanent snow cover (Antarctica, Greenland) corrected for the non-Lambertian snow reflectance.

Over continents, a more realistic rms for snow/ice albedo would be at least 10–15%. (2) Errors do not include a $\pm 3\%$ uncertainty in absolute flux attributable to extra-terrestrial solar flux. (3) The uncertainty in long-term trend is 1%/decade [Herman *et al.*, 1996], caused primarily by total ozone uncertainties. (4) The flux at 310 nm has roughly the same ozone response as the erythema-weighted flux. Uncertainties in spectral flux at other wavelengths for $\theta_0 < 50^\circ$ can be approximately scaled relative to 310 nm by using the following factors: 2 (305 nm), 4 (300 nm), 6 (295 nm). For $\theta_0 > 50^\circ$, the uncertainties in spectral flux cannot be scaled because of the Umkehr effect. (5) The tropospheric ozone variation produces two types of errors in estimation of UVB flux from TOMS. The error listed under “tropospheric profile” was discussed in section 2.4 of this paper. An additional error discussed by Klenk *et al.* [1982] affects the retrieval of TOMS total ozone. This error is included in the 2% uncertainty of TOMS total ozone. (6) Under polluted conditions, errors can result from the presence of SO₂ [Bais *et al.*, 1993; Fioletov and Evans, 1997]. These errors are of roughly the same magnitude as errors due to tropospheric ozone (rms variation in SO₂ is between 1 and 2 DU, but SO₂ is 2–3 times more absorbing than ozone in UVB).

4.2. Nonabsorbing Aerosol Effect

Detailed radiative transfer calculations show that the transmission of UV flux through nonabsorbing aerosols and clouds can be predicted accurately using backscattered radiances measured at nonozone-absorbing UVA wavelengths (TOMS wavelengths at 360 or 380 nm are used for this purpose). Since the cloud transmission function is more complicated than that for nonabsorbing aerosols, we will deal with cloud transmission in a following paper. Here we limit our discussions to nonabsorbing aerosol transmission.

One of the simplest ways of estimating the surface flux attenuation (η) in the presence of nonabsorbing aerosols is to compute from TOMS radiances a quantity that has been referred to in the TOMS literature as Lambert-equivalent reflectivity (LER). The concept of LER was developed by Dave [1978] (see also Klenk *et al.* [1982], Bhartia *et al.* [1993], Eck *et al.* [1995], Herman *et al.* [1996, 1997], and Torres *et al.* [1997]), who showed that the contribution of nonabsorbing aerosols to the backscattered radiances can be modeled accurately using this concept. The LER is derived by assuming that the effect of aerosols (and clouds) on the backscattered radiances in UV is similar to that of a Lambertian reflecting surface with enhanced albedo, the enhancement (over the background) being proportional to the amount of Mie scatterers (clouds plus aerosols) present. Under cloud-free conditions the operational TOMS algorithm derives LER by solving the following equation

at 380 nm (or 360 nm) for the radiation reaching the instrument:

$$I(\theta, \theta_0, \varphi, P_s, R) = I_0(\theta, \theta_0, \varphi, P_s) + RT(\theta, \theta_0, P_s)/[1 - RS_b] \quad (4)$$

where R is the estimated value of LER, P_s is the surface pressure, I_0 is the radiation reaching the instrument from a pure Rayleigh atmosphere with zero surface reflectivity, RT is the amount of radiation reflected by the surface that reaches the satellite, and $[1 - RS_b]^{-1}$ accounts for the multiple reflections from the surface. For the wavelengths of interest, I_0 , S_b , and T are estimated assuming a purely Rayleigh atmosphere with no gaseous absorption and no Mie scattering. (A small correction is made for rotational-Raman scattering, using the procedure described by Joiner *et al.* [1995]).

In the presence of nonabsorbing aerosols, R becomes greater than R_s , the true surface reflectivity. The UV flux attenuation (spectrally flat) can be estimated from the following equation [Eck *et al.*, 1995; Herman *et al.*, 1996; Krotkov *et al.*, 1997]:

$$\eta = 0.5(R - R_s)/(0.5 - R_s) \quad (5)$$

where R_s is based on minimum R values measured by Nimbus 7/TOMS [Eck *et al.*, 1995; Herman and Celarier, 1997]. Equation (5) accounts for a decrease in the Earth surface contribution to total scene reflectance as aerosol optical depth increases [Eck *et al.*, 1995]. Figure 13 shows that for nonabsorbing aerosols and $R_s = 0.05$, the relationship between η and $(R - 0.05)/0.9$ is linear with slope close to unity. Similar calculations at different measurement geometries indicate that (5) can be used to estimate η to about 10–20% accuracy for snow- and cloud-free conditions. For typical values of $\eta = 0.05$ (see Figure 8 for $\tau_a < 0.5$), this amounts to less than 1% error in estimating surface flux at all UV wavelengths.

An additional error occurs due to error in the assumed climatological surface reflectivity [Herman and Celarier, 1997]. For example, if the real albedo of the surface is 0.06 and the TOMS algorithm uses the climatological value of $R_s = 0.05$, the true surface flux will be enhanced by 0.4% (Table 3) compared to the TOMS estimated clear sky flux (1). Both TOMS 360 and 380 nm reflectivity measurements are also enhanced by ~ 0.01 , which is attributed to the presence of aerosols. The aerosol adjustment will reduce the estimated flux by $\eta \approx (R - 0.05)/0.9 = 0.01$, instead of increasing it by 0.4%. Therefore the overall flux error for a 1% rms error in surface reflectivity is $\sim 1.4\%$. Figure 12 shows an rms scatter of $\sim 5\%$ about the

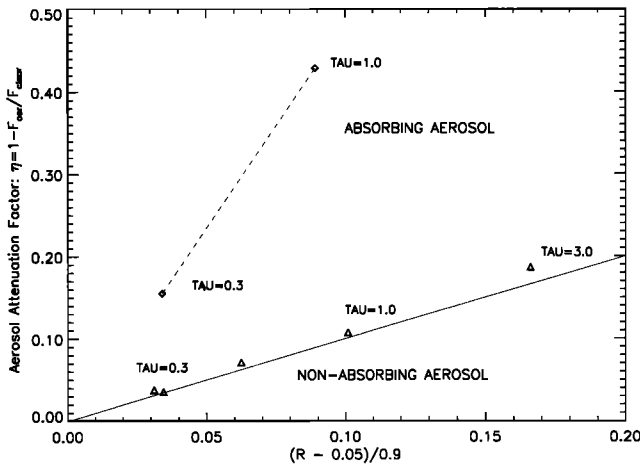


Figure 13. Aerosol attenuation factor $\eta(\lambda) = 1 - F_{\text{aer}}(\lambda)/F_{\text{clear}}(\lambda)$ at 325 nm for nonabsorbing (triangles) and absorbing (diamonds) aerosols as a function of the TOMS Lambert-equivalent reflectivity, $(R - 0.05)/0.9$ (the true surface reflectivity $R_s = 0.05$). Solar zenith angle is 50° , satellite zenith angle 32° , and azimuth 90° .

mean bias of 8%. The 5% rms scatter is an indication of the precision for the cloud-free, snow/ice-free TOMS estimate of the absolute surface flux near 324 nm in the presence of weakly absorbing aerosols.

Larger errors occur when aerosol is present over a snow/ice surface, where $R \approx R_s$ with or without nonabsorbing aerosols. Thus TOMS loses the ability to detect such aerosols and, consequently, can give an incorrect estimate of the surface flux. The snow/ice errors are the subject of a separate study. Larger errors also occur when the underlying surface is highly non-Lambertian, for example, affected by the sea glint. Under these conditions the method would falsely identify the enhanced value of R due to sea glint as aerosols, significantly underestimating the flux. In the operational TOMS algorithm these scenes are identified by the measurement geometry and a land/sea mask and deleted from processing.

4.3. Absorbing Aerosol Effect

Ground-based and satellite measurements in many locations indicate the presence of continental dust and carbonaceous aerosols [Herman et al., 1997] that have significant UV absorption (Figures 8, 9). The LER method described above fails under these conditions for several reasons. First, the slope of η dependence on LER ($\partial\eta/\partial x$, $x = 0.5(R - R_s)/(0.5 - R_s)$) becomes greater than unity even for weakly absorbing aerosols (Figure 13). This causes aerosol optical thickness to be underestimated with respect to the nonabsorbing aerosol and surface flux to be overestimated. Second, Saharan dust aerosols tend to decrease the LER values with respect to the true surface reflectivity: $R - R_s < 0$ [Herman and Celarier, 1997]. This causes negative values of η if the nonabsorbing aerosol model is used (5). Finally, Figures 8, 9, and 13 show that the surface flux is reduced by significantly enhanced attenuation of radiation passing through absorbing aerosols. The LER method cannot capture this effect.

Recently, a technique has been developed to detect absorbing aerosols [Herman et al., 1997; Torres et al., 1997], using TOMS measurements at two wavelengths (340 and 380 nm on Nimbus 7/TOMS instrument (1978–1993), 331 and 360 nm on

Earth Probe (EP) TOMS instrument (July 1996 to present)) where ozone absorption is weak. This unique method takes advantage of the fact that the strong Rayleigh molecular scattering in UV interacts with absorbing aerosols in such a manner as to allow the derivation of both optical depths and single-scattering albedos if there is no clouds and the altitude of aerosol is known [Torres et al., 1997]. In addition, the method allows to detect nonabsorbing aerosols with effective radius close to $0.1 \mu\text{m}$.

By monitoring the spectral slope and magnitude of the back-scattered radiance changes, the operational TOMS algorithm estimates a quantity called UV-absorbing aerosol index (AI) [Hsu et al., 1996; Herman et al., 1997; Torres et al., 1997]. As described by Torres et al. [1997], at near-UV wavelengths (330–400 nm), the AI has the opposite sign for absorbing and nonabsorbing aerosols. Plate 1 shows a TOMS global map of the AI from September 3, 1987. One sees the effects of smoke from a west coast Canadian forest fire that is moving in the southwesterly direction, biomass burning in South America and southern Africa, and desert dust blowing both east and west from the Saharan region of Africa (see also Herman et al. [1997, Figure 2] where this figure is described in detail).

Hsu and Herman [1998] compared EP/TOMS AI data with Sun photometer Aerosol Robotic Network (AERONET) aerosol optical depth measurements [Holben et al., 1996] on cloud-free days in 1996 and 1997. For nine sites affected by smoke (from biomass burning in South America and southern Africa) and African desert dust (Plate 1), they found a linear relationship between AI and τ_a :

$$\text{AI} = a + b\tau_a \quad (6)$$

where the slope b at 340 nm ranges from 0.75 for South American smoke (Los Fieros, Bolivia) to 1.1 for southern African smoke (Mongu, Zambia). For summertime dust, b at 440 nm ranges from 2.6 at Barbados (13°N , 60°W) to 3.3 for the Bidi Bahn, Burkina Faso (14°N , 2.4°W), and Banizoumbou, Niger (13.5°N , 2.6°E), with lower values in the fall/winter/spring seasons. The seasonal dependence is attributed to the changes in the dust layer height. The intercept a ranges from -0.5 to $+0.1$, depending on location and season of the year. Even though the negative intercepts occur frequently, there is not enough data to insure that the a values are statistically different from 0. Radiative transfer calculations yield negative AI values for nonabsorbing sulfate aerosols in the wide range of particle sizes [Torres et al., 1997]. Therefore if the apparent negative intercepts are confirmed by additional future measurements, they can be explained by the presence of nonabsorbing boundary layer aerosols (haze, sulfate). It was also shown that aerosols at low altitudes (below 2 km) tend to produce small values of AI even for strongly absorbing aerosols. This is not a limitation for biomass burning smoke or desert dust aerosols, because these aerosols are transported by winds high enough in the troposphere (between 2 and 5 km). For these aerosols, $a \approx 0$, and the slope b increases with aerosol absorption but decreases with decreasing aerosol altitude.

Since AI is sensitive to the same aerosol parameters (τ_a , ω), which affect the surface UV flux (3), it is expected that the η and AI would have a close relationship. (Except for the complication caused by the fact that some of the satellite-received photons are scattered from above the aerosol layer and therefore do not see the aerosols, while all the photons reaching the surface are affected by aerosols. Estimation of this geometric factor requires the knowledge of aerosol layer altitude). Here

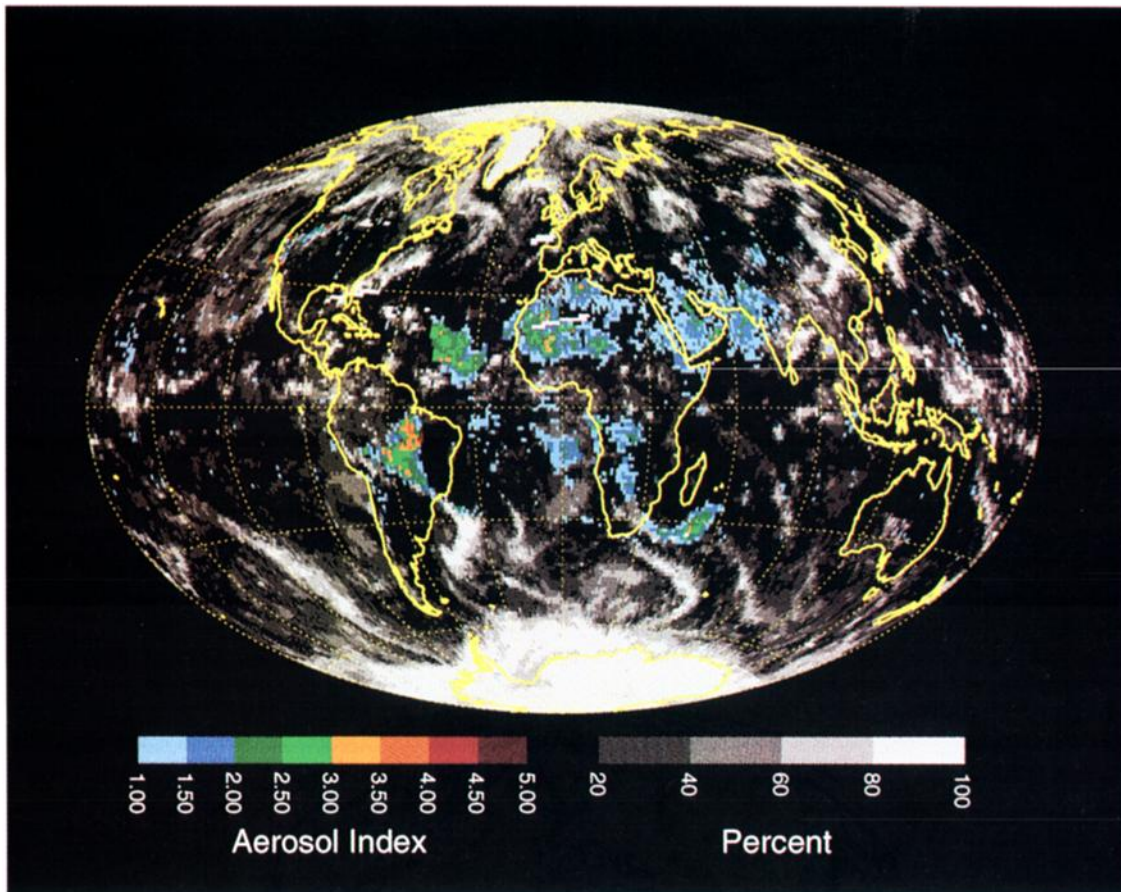


Plate 1. Global map of the Nimbus 7/TOMS aerosol index (AI > 1) (340/380) on September 3, 1987. Positive AI indicates the presence of UV-absorbing aerosols. One sees smoke from a west coast Canadian forest fire and from biomass burning in South America and Africa, and desert dust blowing both east and west from the Saharan region of Africa. AI increases with aerosol optical depth, single-scattering coalbedo ($1 - \omega$), and altitude (color scale). The TOMS band at 380 nm is used to measure UV reflectivity of water clouds and the Earth's surface (grey scale).

we estimate the relationship between η and AI based on radiative transfer modeling assuming a single absorbing aerosol layer between 2 and 4 km ($a = 0$):

$$\eta = 1 - \exp[-k/b \text{ AI}] \quad (7)$$

Although both k and b are strong increasing functions of the aerosol absorption ($1 - \omega$), the conversion factor (k/b) is a weak function of aerosol absorption. Our calculations have shown that for both dust and smoke aerosols in tropics, $k/b = 0.2$ – 0.3 (solar zenith angle between 0° and 30° for local noon TOMS overpasses). Plate 2 shows a preliminary estimate of η derived from the TOMS AI map (Plate 1) based on (7) and constant conversion factor $k/b = 0.25$. The map shows that aerosol absorption can produce very large reductions in UV flux ($\sim 50\%$) in certain parts of the world (with larger attenuation caused by lower-altitude aerosols). These estimates are consistent with TOMS optical depth and single-scattering albedo retrievals for the same regions [Torres *et al.*, 1997].

In the future, more accurate estimates for the conversion of AI to η will be made, which will be based on different look-up tables for different types of aerosols, locations, and seasons (note different k values in Table 1; see also Figure 8). The dependence on solar zenith angle and satellite-viewing geometry can be easily taken into account. The altitude of aerosol

cannot be directly derived from the TOMS measurements alone. For cloud-free conditions and assuming aerosol altitude, Torres *et al.* [1997] inferred τ_{TOMS} and ω_{TOMS} directly from the TOMS radiances for given aerosol models (smoke, dust). By requiring that τ_{TOMS} match the Sun photometer measured τ , one can estimate the altitude of the aerosol layer. The preliminary comparisons of τ_{TOMS} with Sun photometer τ measurements from Dakar have shown that the initial assumption about the dust aerosol altitude (between 2 and 4 km) is not too far from reality [Torres *et al.*, 1997].

An important feature to note is that the map is limited to $\eta = 0.2$ (AI > 1). This is because of lack of sensitivity in the TOMS technique to reliably detect smaller amounts of absorbing aerosols. Although further work may improve the sensitivity of the estimation procedure, it is unlikely that TOMS AI technique will be able to detect weakly absorbing aerosols near the surface, often found in urban atmospheres [Liu *et al.*, 1991]. These aerosols can still be detected using single reflectivity channel (380 nm or 360 nm) at any altitude given all limitations of the LER method (see section 4.2). The LER method can provide an estimate of the aerosol optical depth for a weakly absorbing aerosol if the single-scattering albedo is known.

Since the operational TOMS UV-flux algorithm does not

N7/TOMS, Estimated Aerosol Attenuation for 09/03/87

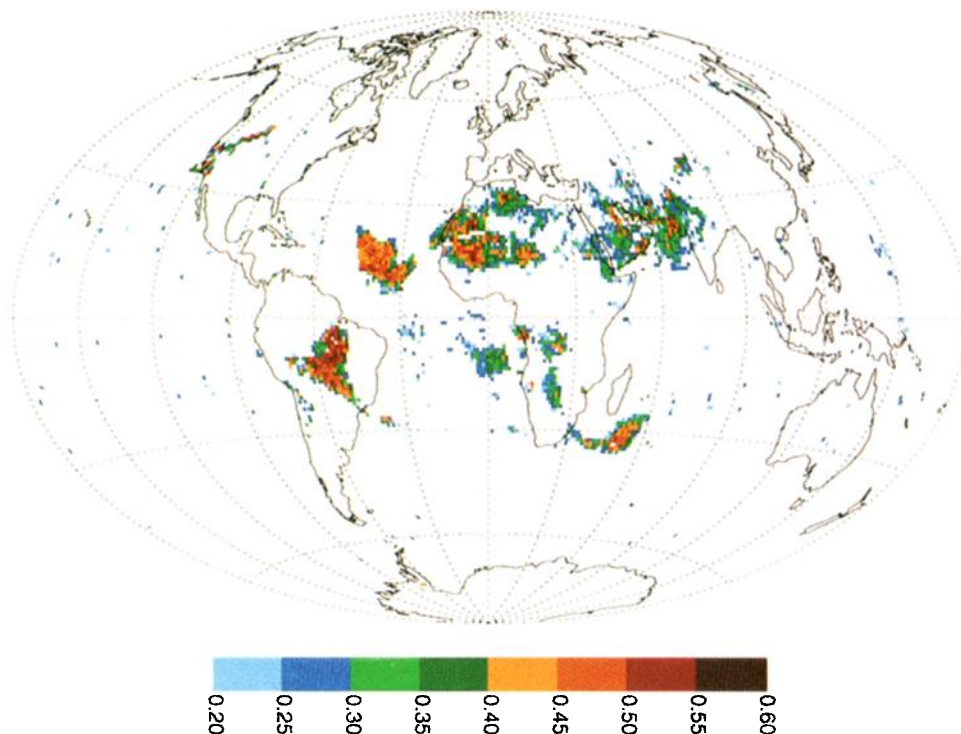


Plate 2. Global map of aerosol UV-flux attenuation factor, $\eta = 1 - F_{\text{acr}}/F_{\text{clear}} = 1 - \exp\{-(k/b)AI\}$, estimated from the aerosol index map in Plate 1. The conversion factor, $k/b = 0.25$, was obtained from the clear sky radiative transfer calculations, assuming single aerosol layer (dust or smoke) between 2 and 4 km and solar zenith angle 30° . The map shows that aerosol absorption can produce very large reductions in UV flux ($\sim 50\%$) in certain parts of the world.

correct the estimated surface UV flux for absorbing aerosols, the errors can range from a few percent overestimation to 50% or more depending on the amount of UV-absorbing aerosols present at a given location. With the incorporation of the TOMS aerosol index in the estimation procedure the maximum errors can be reduced to 10–15%, but smaller errors would still remain, for the reasons mentioned above.

5. Conclusions

We have demonstrated that with the knowledge of extraterrestrial solar flux and in the absence of clouds and UV-absorbing aerosols, satellite (TOMS) measurements of total column ozone and 360 nm (or 380 nm) radiances, combined with radiative transfer calculations, can provide estimates of surface spectral UV flux to accuracies comparable to that of typical ground-based measurements. The percentage errors range from $\sim 4\%$ at 305 nm, $\sim 8\%$ at 300 nm, and $\sim 12\%$ at 295 nm. These errors are caused primarily by uncertainties in satellite-measured tropospheric ozone (and other pollutions). At larger solar zenith angles ($\theta_0 > 50^\circ$), additional errors occur due to ozone profile shape effects. Since most of these errors are random, monthly mean flux and long-term trends can be derived with much greater accuracies.

One of the largest sources of uncertainty in deriving the UV flux from satellite data for cloud- and snow-/ice-free conditions comes from UV-absorbing aerosols. The spatial and temporal variability of these aerosols are poorly known. A newly developed technique using TOMS data allows estimation of strongly absorbing aerosols, indicating that over parts of the Earth,

aerosols can cause 50% or more reduction in the UV flux. However, the technique currently does not have the sensitivity to detect the more prevalent weakly absorbing aerosols and absorbing aerosols at low altitudes.

Since the uncertainty due to UV-absorbing aerosols is a large remaining source of error in determining surface UV irradiance spectra from space, a high priority for the TOMS surface UV validation program is understanding the variability of the aerosol (and cloud) attenuation factor (η). Both ground-based measurements and model calculations indicate that η is weakly wavelength dependent under most conditions. Understanding the behavior of η could therefore be achieved relatively inexpensively by deploying many broadband UVA instruments at different sites around the world.

Acknowledgments. We thank the members of the TOMS OPT team for producing TOMS aerosol and surface UV flux data sets. In particular, the first author wishes to thank Tom Eck, Omar Torres, Christina Hsu, Edward Celarier, and Gordon Labow for many useful discussions on different aspects of this study, Colin Seftor for help with TOMS data, Charlie Wellemeyer for excellent comments on the manuscript, and the reviewers for valuable improvements. The work was supported by the NASA TOMS program.

References

- Anderson, D. E., and S. A. Lloyd, Polar twilight UV-Visible radiation field: Perturbations due to multiple scattering, ozone depletion, stratospheric clouds, and surface albedo, *J. Geophys. Res.*, **95**, 7429–7434, 1990.
- d’Almeida, G. A., On the variability of desert dust radiative characteristics, *J. Geophys. Res.*, **92**, 3017–3026, 1987.

- Bais, A. F., C. S. Zerefos, C. Meleti, I. C. Ziomas, and K. Tourpali, Spectral measurements of solar UVB radiation and its relations to total ozone, SO_2 , and clouds, *J. Geophys. Res.*, **98**, 5199–5204, 1993.
- Bass, A. M., and R. J. Paur, The ultraviolet cross-sections of ozone, I, II, in *Atmospheric Ozone*, edited by C. Z. Zerefos and A. Ghaz, pp. 606–616, D. Reidel, Norwell, Mass., 1985.
- Bates, D. R., Rayleigh scattering by air, *Planet. Space Sci.*, **32**, 785–790, 1984.
- Beyer, K. D., A. R. Ravishankara, and E. R. Lovejoy, Measurements of UV refractive indices and densities of $\text{H}_2\text{SO}_4/\text{H}_2\text{O}$ and $\text{H}_2\text{SO}_4/\text{HNO}_3/\text{H}_2\text{O}$ solutions, *J. Geophys. Res.*, **101**, 14,519–14,524, 1996.
- Bhartia, P. K., J. Herman, P. D. McPeters, and O. Torres, Effect of Mount Pinatubo aerosols on total ozone measurements from backscatter ultraviolet (BUV) experiments, *J. Geophys. Res.*, **98**, 18,547–18,554, 1993.
- Blumthaler, M., and W. Ambach, Solar UVB-albedo of various surfaces, *Photochem. Photobiol.*, **48**, 85–88, 1988.
- Blumthaler, M., A. R. Webb, G. Seckmeyer, A. F. Bais, M. Huber, and B. Mayer, Simultaneous spectroradiometry: A study of solar UV irradiance at two altitudes, *Geophys. Res. Lett.*, **21**, 2805–2808, 1994.
- Brueckner, G. E., et al., The Solar Ultraviolet Spectral Irradiance Monitor (SUSIM) onboard the Upper Atmospheric Research Satellite (UARS), *J. Geophys. Res.*, **98**, 10,695–10,711, 1993.
- Bruhl, C., and P. J. Crutzen, On the disproportional role of tropospheric ozone as a filter against solar UV-B radiation, *Geophys. Res. Lett.*, **16**, 703–706, 1989.
- Cebula, R. P., et al., Observations of the solar irradiance in the 200–350 nm interval during the ATLAS-1 mission: A comparison among three sets of measurements—SSBUV, SOLSPEC, and SUSIM, *Geophys. Res. Lett.*, **23**, 289–2292, 1996.
- Chubarova, N. Y., N. A. Krotkov, I. V. Geogdzaev, T. V. Kondranin, and V. U. Khatatov, Spectral Irradiance: The effects of ozone, cloudiness and surface albedo, in *IRS'96: Current Problems in Atmospheric Radiation*, edited by W. L. Smith and Knut Stamnes, pp. 881–885, A. Deepak, Hampton, Va., 1997.
- Dave, J. V., Meaning of successive iteration of the auxiliary equation of radiative transfer, *Astrophys. J.*, **140**, 1,292–1,303, 1964.
- Dave, J. V., Effect of aerosols on the estimation of total ozone in an atmospheric column from the measurements of its ultraviolet radiance, *J. Atmos. Sci.*, **35**, 899–911, 1978.
- DeLand, M. T., and R. P. Cebula, NOAA-11 SBUV/2 solar spectral irradiance measurements 1989–1994, II, Results, validation, and comparisons, *J. Geophys. Res.*, in press, 1997.
- Diffey, B. L., A. T. Green, M. J. Loftus, G. J. Johnston, and P. S. Lee, A portable instrument for measuring ground reflectance in the ultraviolet, *Photochem. Photobiol.*, **61**, 68–70, 1995.
- Eck, T. F., P. K. Bhartia, P. H. Hwang, and L. L. Stowe, Reflectivity of Earth's surface and clouds in ultraviolet from satellite observations, *J. Geophys. Res.*, **92**, 4287–4296, 1987.
- Eck, T. F., P. K. Bhartia, and J. B. Kerr, Satellite estimation of spectral UVB irradiance using TOMS derived ozone and reflectivity, *Geophys. Res. Lett.*, **22**, 611–614, 1995.
- Feister, U., and R. Grewe, Spectral albedo measurements in the UV and visible region over different types of surfaces, *Photochem. Photobiol.*, **62**, 736–744, 1995.
- Fioletov, V. E., and W. F. J. Evans, The influence of ozone and other factors on surface radiation, in *Ozone Science: A Canadian Perspective on the Changing Ozone Layer*, edited by D. I. Wardle, J. B. Kerr, C. T. McElroy, and D. R. Francis, *Environ. Can.*, Rep. CARD 97-3, pp. 73–90, Atmos. Environ. Serv., Downsview, Ontario, Canada, 1997.
- Fioletov, V. E., J. B. Kerr, and D. I. Wardle, The relationship between total ozone and spectral UV irradiance from Brewer observations and its use for derivation of total ozone from UV measurements, *Geophys. Res. Lett.*, **24**, 2997–3000, 1997.
- Frederick, J. E., and D. Lubin, The budget of biologically active ultraviolet radiation in the Earth-atmosphere system, *J. Geophys. Res.*, **93**, 3825–3832, 1988.
- Grenfell, T. C., S. G. Warren, and P. C. Mullen, Reflection of Solar Radiation by the Antarctic snow surface at ultraviolet, visible, and near-infrared wavelengths, *J. Geophys. Res.*, **99**, 18,669–18,684, 1994.
- Herman, B. M., and S. R. Browning, A numerical solution to the equation of radiative transfer, *J. Atmos. Sci.*, **22**, 559–566, 1965.
- Herman, J. R., and E. A. Celarier, Earth Surface reflectivity climatology at 340 nm to 380 nm from TOMS data, *J. Geophys. Res.*, **102**, 28,003–28,012, 1997.
- Herman, J. R., and D. Larko, Low ozone amounts during 1992 and 1993 from Nimbus 7 and Meteor 3 total ozone mapping spectrometers, *J. Geophys. Res.*, **99**, 3483–3496, 1994.
- Herman, J. R., P. K. Bhartia, J. Ziemke, Z. Ahmad, and D. Larko, UV-B radiation increases (1979–1992) from decreases in total ozone, *Geophys. Res. Lett.*, **23**, 2117–2120, 1996.
- Herman, J. R., P. K. Bhartia, O. Torres, C. Hsu, C. Seftor, and E. Celarier, Global distribution of UV-absorbing aerosols from Nimbus 7/TOMS data, *J. Geophys. Res.*, **102**, 16,911–16,922, 1997.
- Holben B. N., et al., Effect of dry-season biomass burning on Amazon Basin aerosol concentrations and optical properties, 1992–1994, *J. Geophys. Res.*, **101**, 19,465–19,481, 1996.
- Hsu, N. C., and J. R. Herman, Comparisons of the TOMS aerosol index with Sun photometer aerosol optical thickness, *J. Geophys. Res.*, in press, 1997.
- Hsu, N. C., J. R. Herman, P. K. Bhartia, C. J. Seftor, O. Torres, A. M. Thompson, J. R. Gleason, T. F. Eck, and B. N. Holben, Detection of biomass burning smoke from TOMS measurements, *Geophys. Res. Lett.*, **23**, 745–748, 1996.
- International Arctic Science Committee (IASC) Effects of increased ultraviolet radiation in the Arctic, An interdisciplinary report on the state of knowledge and research need, *LASC Rep. N2*, Oslo, 1996.
- Joiner, J., P. K. Bhartia, R. C. Cebula, E. Hilsenrath, R. D. McPeters, and H. Park, Rotational Raman scattering (Ring effect) in satellite backscatter ultraviolet measurements, *Appl. Opt.*, **34**, 4513–4525, 1995.
- Kerr, J. B., Observed dependencies of atmospheric UV radiation and trends, in *NATO ASI Series*, vol. I 52, edited by C. S. Zerefos and A. F. Bais, Springer-Verlag, New York, 1997.
- Klenk, K. F., P. K. Bhartia, A. J. Fleig, V. G. Kaveeshwar, R. D. McPeters, and P. M. Smith, Total ozone determination from the backscattered ultraviolet (BUV) experiment, *J. Appl. Meteorol.*, **21**, 1672–1684, 1982.
- Klenk, K. F., P. K. Bhartia, E. Hilsenrath, and A. Fleig, Standard ozone profiles from balloon and satellite data sets, *J. Clim. Appl. Meteorol.*, **22**, 2012–2022, 1983.
- Krotkov, N. A., P. K. Bhartia, J. Herman, E. Celarier, and T. Eck, Estimates of spectral UVB irradiance from the TOMS instrument: Effects of clouds and aerosols, in *IRS'96: Current Problems in Atmospheric Radiation*, edited by W. L. Smith and Knut Stamnes, 873–876, A. Deepak, 1997.
- Labow, G. J., J. R. Herman, E. Celarier, N. A. Krotkov, and J. B. Kerr, Estimates of Spectral UV irradiance from the TOMS Instruments: Comparisons with ground-based measurements, *J. Geophys. Res.*, in press, 1998.
- Leffell, D. J., and D. E. Brash, *Sunlight and Skin Cancer*, pp. 52–59, Sci. Am., New York, 1996.
- Liu, S. C., S. A. McKeen, and S. Madronich, Effect of anthropogenic aerosols on biologically active ultraviolet radiation, *Geophys. Res. Lett.*, **18**, 2265–2268, 1991.
- Long, C. S., A. J. Miller, H. T. Lee, J. D. Wild, R. C. Przywarty, and D. Hufford, Ultraviolet index forecasts issued by the National Weather Service, *Bull. Am. Meteorol. Soc.*, **77**, 729–747, 1996.
- Lubin, D., and E. H. Jensen, Effects of clouds and stratospheric ozone depletion on ultraviolet radiation trends, *Nature*, **377**, 710–713, 1995.
- Lubin D., P. Ricchiazzi, C. Gautier, and R. H. Whritner, A method for mapping Antarctic surface ultraviolet radiation using multispectral satellite imagery, in *Ultraviolet Radiation in Antarctica: Measurements and Biological Effects*, *Antarct. Res. Ser.*, vol. 62, edited by C. S. Weiler and P. A. Penhale, pp. 53–82, AGU, Washington, D. C., 1994.
- Madronich, S., Implications of recent total ozone measurements for biologically active ultraviolet radiation reaching the Earth's surface, *Geophys. Res. Lett.*, **19**, 37–40, 1992.
- Madronich, S., The atmosphere and UV-B radiation at ground level, in *Environmental UV Photobiology*, edited by A. R. Young et al., pp. 1–39, Plenum Press, New York, 1993.
- Mateer, C. L., On the information content of Umkehr observations, *J. Atmos. Sci.*, **22**, 370–381, 1965.
- Mayer, B., G. Seckmeyer, and A. Kylling, Systematic long-term comparison of spectral UV measurements and UVSPEC modeling results, *J. Geophys. Res.*, **102**, 8755–8767, 1997.
- McKenzie, R. L., M. Kotkamp, and W. Ireland, Upwelling UV spectral irradiances and surface albedo measurements at Lauder, New Zealand, *Geophys. Res. Lett.*, **23**, 1757–1760, 1996.

- McPeters, R. D., et al., Total ozone Mapping Spectrometer (TOMS) Data Products User's Guide, *NASA Ref. Publ. 1384*, 1996.
- Meerkötter, R., B. Wissinger, and G. Seckmeyer, Surface UV from ERS-2/GOME and NOAA/AVHRR data: A case study, *Geophys. Res. Lett.*, **24**, 1939–1942, 1997.
- Patterson, E. M., D. A. Gillette, and B. H. Stockton, Complex index of refraction between 300 and 700 nm for Saharan aerosols, *J. Geophys. Res.*, **82**, 3153–3160, 1977.
- Rottman, G. J., et al., Solar Stellar Irradiance Comparison Experiment: Instrument design and operation, *J. Geophys. Res.*, **98**, 10,667–10,678, 1993.
- Schütz, L., Long-range transport of desert dust with special emphasis on the Sahara, *Ann. N. Y. Acad. Sci.*, **338**, 515–532, 1980.
- Scientific Committee on Problems of the Environment (SCOPE), *Effects of Increased Ultraviolet Radiation on Biological Systems*, Paris, 1992.
- SCOPE, Effects of increased ultraviolet radiation on global ecosystems, Paris, 1993.
- Shaw, G. E., Considerations on the origin and properties of the Antarctic aerosol, *Rev. Geophys.*, **8**, 1983–1998, 1979.
- Smith, R. C., et al., Ozone depletion: Ultraviolet radiation and phytoplankton biology in Antarctic waters, *Science*, **255**, 952–959, 1992.
- Sokolik, I., A. Andronova, and T. C. Johnson, Complex refractive index of atmospheric dust aerosols, *Atmos. Environ.*, **27**(A), 2495–2502, 1993.
- Stamnes, K., S.-C. Tsay, and K. Jayaweera, Numerically stable algorithm for discrete-ordinate-method radiative transfer in multiple scattering and emitting layered media, *Appl. Opt.*, **27**, 2502–2509, 1988.
- Stolarski, R. S., P. Bloomfield, R. D. McPeters, and J. R. Herman, Total ozone trends deduced from Nimbus 7 TOMS data, *Geophys. Res. Lett.*, **18**, 1015–1018, 1991.
- Torres, O., P. K. Bhartia, J. R. Herman, and Z. Ahmad, Derivation of aerosol properties from satellite measurements of backscattered ultraviolet radiation, Theoretical basis, *J. Geophys. Res.*, in press, 1998.
- United Nations Environment Programme (UNEP), *Environmental Effects of Stratospheric Ozone Depletion—1994 Assessment*, edited by J. C. van der Leun, A. H. Teramura, and M. Tevini, Nairobi, 1994.
- Weihs, P., and A. R. Webb, Accuracy of spectral UV model calculations, 2, Comparison of UV calculations with measurements, *J. Geophys. Res.*, **102**, 1551–1560, 1997.
- Weiler, C. S., and P. A. Penhale (Eds.), *Ultraviolet Radiation in Antarctica: Measurements and Biological Effects*, *Antarct. Res. Ser.*, vol. 62, 257 pp., AGU, Washington, D. C., 1994.
- Wieser, M., The global digital terrain model TUG87, internal report on set-up, origin and characteristics, Inst. of Math. Geod., Tech. Univ. of Graz, Graz, Austria, 1987.
- Wellemeyer, C. G., S. L. Taylor, G. Jaross, M. T. DeLand, C. J. Seftor, G. Labow, T. J. Swisler, and R. P. Cebula, Final report on Nimbus-7 TOMS version 7 calibration, NASA contractor report 4717, 48 pp., 1996.
- Wellemeyer, C. G., S. L. Taylor, C. J. Seftor, R. D. McPeters, and P. K. Bhartia, A correction for total ozone mapping spectrometer profile shape errors at high latitude, *J. Geophys. Res.*, **102**, 9029–9038, 1997.
- Woods, T. N., et al., Validation of the UARS solar ultraviolet irradiances: Comparison with the ATLAS 1 and 2 measurements, *J. Geophys. Res.*, **101**, 9541–9569, 1996.
- World Meteorological Organization (WMO), Radiation Commission, A preliminary cloudless standard atmosphere for radiation computations, *WCP-112, WMO/TD-24*, 53 pp., World. Clim. Res. Programme, Int. Assoc. for Meteorol. and Atmos. Phys., Geneva, 1986.
- WMO, Scientific Assessment of Ozone Depletion: 1994, Global Ozone Research and Monitoring Project, *WMO Rep. N 37*, Geneva, 1995.
- P. K. Bhartia and J. R. Herman, Laboratory for Atmospheres, NASA Goddard Space Flight Center, Greenbelt, MD 20771.
- V. Fioletov and J. Kerr, Atmospheric Environmental Service, Downsview, Ontario, Canada.
- N. A. Krotkov, Raytheon STX Corporation, 4400 Forbes Blvd., Lanham, MD 20706-4392. (e-mail: krotkov@hoss.stx.com)

(Received September 11, 1997; revised January 15, 1998; accepted January 15, 1998.)